

Vacancy-Defect Modulated Pathway of Photoreduction of CO₂ on Quaternary Single Atomically Thin AgInP₂S₆ Sheets toward Boosting Efficient and Selective Production of Value-Added Olefiant Gas

Yong Zhou (✉ zhouyong1999@nju.edu.cn)

Nanjing University

Zhigang Zou

Nanjing University

Wa Gao

Nanjing University

Xiaoyong Wang

Nanjing University

Qing Shen

Huichao He

Southwest University of Science and Technology <https://orcid.org/0000-0003-1193-1129>

Xiong Yujie

University of Science and Technology of China

Jinlan Wang

Southeast University

Li Shi

Southeast University

Yong Yang

Nanjing University of Science and Technology <https://orcid.org/0000-0001-8872-2777>

Zhenxiang Cheng

Institute for Superconducting & Electronic Materials, Australian Institute of Innovative Materials, University of Wollongong, Innovation Campus, Squires Way, North Wollongong, NSW 2500

<https://orcid.org/0000-0003-4847-2907>

Xiaoning Li

Institute for Superconducting and Electronic Materials, University of Wollongong

<https://orcid.org/0000-0001-5991-0955>

Keywords: Facile Ultrasonic Exfoliation, Photocatalytic Conversion, Sulfur Defect Engineering, Dominant Generation of Ethene

Posted Date: February 24th, 2021

DOI: <https://doi.org/10.21203/rs.3.rs-225023/v1>

License:  This work is licensed under a Creative Commons Attribution 4.0 International License.

[Read Full License](#)

Version of Record: A version of this preprint was published at Nature Communications on August 6th, 2021. See the published version at <https://doi.org/10.1038/s41467-021-25068-7>.

Vacancy-Defect Modulated Pathway of Photoreduction of CO₂ on Quaternary Single Atomically Thin AgInP₂S₆ Sheets toward Boosting Efficient and Selective Production of Value-Added Olefiant Gas

Wa Gao,^{1,‡} Shi Li,^{3,‡} Huichao He,² Xiaoning Li,⁵ Zhenxiang Cheng,⁵ Yong Yang,⁶ Jinlan Wang,^{*,3} Qing Shen,⁷ Xiaoyong Wang,¹ Yujie Xiong,^{*,4} Yong Zhou,^{*,1,8} Zhigang Zou^{1,8}

¹ Key Laboratory of Modern Acoustics (MOE), Institute of Acoustics, School of Physics, Eco-materials and Renewable Energy Research Center (ERERC), National Laboratory of Solid State Microstructures, Collaborative Innovation Center of Advanced Microstructures, Nanjing University, Nanjing 210093, China

² State Key Laboratory of Environmental Friendly Energy Materials, Southwest University of Science and Technology, Mianyang 621010, China

³ School of Physics, Southeast University, Nanjing 211189, China

⁴ Hefei National Laboratory for Physical Sciences at the Microscale, Collaborative Innovation Center of Chemistry for Energy Materials (iChEM), School of Chemistry and Materials Science, University of Science and Technology of China, Hefei, Anhui 230026, China

⁵ Institute of Superconducting & Electronic Materials, Innovation Campus, University of Wollongong, Squires Way, North Wollongong, NSW 2500, Australia

⁶ Key Laboratory of Soft Chemistry and Functional Materials (MOE), Nanjing University of Science and Technology, Nanjing 210094, China

⁷ University of Electrocommunication, Grad Sch Informatics and Engineering, 1-5-1 Chofugaoka, Chofu, Tokyo 1828585, Japan.

⁸ School of Science and Engineering, The Chinese University of Hongkong (Shenzhen), Shenzhen, Guangdong 518172, China

‡Gao and Li contributed to the work equally.

* Correspondence and requests for materials should be addressed to Y. Z, J. W, and Y. X. (zhouyong1999@nju.edu.cn, jlwang@seu.edu.cn and yjxiong@ustc.edu.cn)

Abstract

The quaternary AgInP_2S_6 atomic layer with the thickness of ~ 0.70 nm were successfully synthesized through facile ultrasonic exfoliation of the corresponding bulk crystal. The ultrathin sheet exhibits efficiently photocatalytic conversion of CO_2 into CO as a major product and minority of CH_4 and C_2H_4 in the presence of water vapor. The sulfur defect engineering on this atomic layer through a H_2O_2 etch process can excitingly enable to change the CO_2 photoreduction reaction pathway to steer dominant generation of ethene (C_2H_4) important chemical with the yield-based selectivity reaching $\sim 73\%$ and the electron-based selectivity as high as $\sim 89\%$, and the quantum yield of 0.51% at wavelength of 415 nm. Both DFT calculation and *in-situ* FTIR demonstrate as the introduction of S vacancies in AgInP_2S_6 causes the charge accumulation on the Ag atoms near the S vacancies, the exposed Ag sites can thus effectively capture the forming $\ast\text{CO}$ molecules, making the catalyst surface enrich with key reaction intermediates to lower the C-C binding coupling barrier, which facilitates the production of C_2H_4 . Surface photovoltage measurement confirms that atomically ultrathin structure of the exfoliated AgInP_2S_6 can shorten the transfer distance of charge carriers from the interior onto the surface, thus decrease the recombination in body and improve the catalytic efficiency. This work may provide fresh insights into the design of atomically thin photocatalyst framework for CO_2 reduction and establish an ideal platform for reaffirming the versatility of defect engineering in tuning catalytic activity and selectivity.

Introduction

Photocatalytic conversion of CO₂ with H₂O into solar fuels would be like killing two birds with one stone in terms of saving supplying energy and environment, which occurs mostly on the surfaces of semiconductors through complicated processes involving multi-electrons/protons transfer reactions.¹ Photo-driving CO₂ hydrogenation into C₁ species have been well achieved in recent decade,² and our group has exploited a series of promising photocatalysts to converse CO₂ to selectively form specific hydrocarbons, such as Zn₂GeO₄ ultrathin nanoribbons for CH₄,³ atomically thin InVO₄ nanosheets for CO,⁴ and TiO₂-graphene hybrid nanosheets for C₂H₆⁵ and so on. However, the controlled C-C coupling to produce high-value C₂ or C₂₊ products still remains a great challenge. Olefiant gas (Ethylene, C₂H₄) is a chemical source of particular importance due to its high demand in chemical industry. C₂H₄ is usually derived from steam cracking of naphtha under harsh production conditions (800–900 °C). It is definitely desirable for realization of C₂H₄ synthesis through mild and environmentally benign pathways.⁶

Transition metal thio/selenophosphates (TPS) is a broad class of van der Waals layered structures with two sulfur or selenium layers sandwiching a layer of metal ions and P₂ pairs and general compositions of M₄[P₂X₆]⁴⁺, [M²⁺]₂[P₂X₆]⁴⁺, and M¹⁺M³⁺[P₂X₆]⁴⁺, where M¹⁺ = Cu, Ag; M³⁺ = Cr, V, Al, Ga etc. X = S, Se.⁷ Those quaternary compounds exhibit mixed electron–ionic conductivity, promising optical and thermoelectric properties.⁸ AgInP₂S₆ is a typical TPS with a rhombohedral structure and contains a sulfur framework with the octahedral voids filled by Ag, In and P–P triangular patterns. Each AgInP₂S₆ monolayer consists of the [P₂S₆] anionic complex and two metallic cations (Ag and In) located at the center of sulfur near-octahedral polyhedrons connected one with the other by edges. Semiconducting

AgInP₂S₆ crystal possesses appropriate bandgap structure ($E_g = \sim 2.4$ eV), which is favored for visible light absorption.⁹ The low value of the effective mass of electrons and the high value of the effective mass of holes facilitate to accelerate the mobility dynamics of photogenerated electrons onto the surface prior to holes,¹⁰ which may enhance local electron density, benefiting for photo-driving reduction reaction. The centrosymmetry structure of AgInP₂S₆ also enables the photoexcited electrons to distribute on the surface of the layer crystal uniformly,¹¹ which may remarkably reduce the energy barrier for catalytic molecule activation, alter the catalytic reduction pathway, and enhance yield and enrich species of products.

An atomically thin 2D structure is an ideal platform to provide atomic level insights into the structure-activity relationship.¹² Firstly, ultrathin structure allows the photo-generated carriers to easily transfer from the interior to the surface with shortened charge transfer distance, decreasing the bulk recombination. Secondly, large surface exposure renders rich catalytic active sites. Thirdly, transparency resulting from ultrathin thickness helps for light absorption. Creation of vacancy defects in the ultrathin structure can also additionally enrich the reaction intermediates, resulting in low-coordinated atoms on the surface of catalyst, which are known to facilitate to generate multi-carbon species from CO₂ photoreduction.^{13,14}

Herein, we report the synthesis of the AgInP₂S₆ single atomic layer (abbreviated as SAL) of ~ 0.70 nm in thickness through a facile probe sonication exfoliation of the corresponding bulk crystal (abbreviated as BC). The sulfur vacancy (abbreviated as V_S) defects were introduced in the resulting SAL through an etching process with H₂O₂ solution (abbreviated as V_S-SAL), which was prospectively utilized for photocatalytic reduction of CO₂ in the presence of water vapor. While BC and SAL dominantly produce CO, the implemented defect engineering changes the reaction

pathway of the CO₂ photoreduction on V_S-SAL, which allows to steer CO₂ conversion into C₂H₄ with the yield-based selectivity reaching ~73% and the electron-based selectivity as high as ~89%, and the quantum yield of 0.51% at wavelength of 415 nm. Both DFT calculation and *in-situ* FTIR and demonstrate that the key step for the CO production on BC and SAL follows a conventional hydrogenation process of CO₂ to form *COOH, which further couples a proton/electron pair to generate *CO. *CO easily liberates from the defect-free AgInP₂S₆ surface with low absorption energy to become free CO gas. In contrast, the introduction of V_S in AgInP₂S₆ causes the charge accumulation on the Ag atoms near V_S. Thus, the exposed Ag site in V_S-SAL can effectively capture the forming *CO, making the catalyst surface enrich with key reaction intermediates to promote C-C coupling into C₂ species with the low binding energy barrier. This work may provide fresh insights into the design of atomically thin photocatalyst framework for CO₂ reduction and establish an ideal platform for reaffirming the versatility of defect engineering in tuning catalytic activity and selectivity.

Results

Structure characterization of the AgInP₂S₆ related samples. BC was synthesized through physical vapor transport in a two-zone furnace, which displays bright yellowis-brown color (Figure S1a). The SAL was produced through mechanical exfoliation in ethyl alcohol solution through a probe sonication technique. The well-defined Tyndall effect of the resulting transparent solution of SAL indicates high monodispersity of the ultrathin sheets (Figure S1b). Etching of SAL with H₂O₂ solutions allows to deliberately create V_S on the surface of SAL.¹⁵

The powder X-ray diffraction (XRD) pattern of BC and SAL agrees with the simulated one from the crystal structure of ICSD 202185 well with the P₃_{1c} space

group (Figure S2),¹² and no impurity peaks were detected. The stronger SAL peak intensity ratio of (002) to (112) relative to BC indicates that the exfoliation of AgInP₂S₆ occurs along [001] direction. The field emission scanning electron microscopy (FE-SEM) image shows that BC displays an angular shape with an apparent laminar structure (Figures S3a and S3b). The energy dispersive spectroscopy (EDS) spectra demonstrate the uniform spatial distribution of Ag, In, P, and S (Figures S3c-3f). The TEM image of exfoliated SAL displays light contrast of the extremely thin 2D structure (Figure 1a). A magnified TEM image of a vertically standing sheet shows the single-layer with the thickness of ~0.71 nm (Figure 1b). A typical edge-curling sheet as marked with an arrow also particularly shows the thickness of ~0.72 nm of SAL (Figure 1b'), well in agreement with the AgInP₂S₆ monolayer along [002] orientation [$d_{(002)} = 6.68 \text{ \AA}$]. The corresponding atomic force microscopy (AFM) image of SAL also confirms ~0.66-0.73 nm range in thickness (Figure 1c), demonstrating the single atom layer feature. A high-resolution TEM image of SAL reveals that the interplanar d-spacing between the well-defined lattice fringes were examined 0.54 nm, which can be indexed to (010) (Figure 1d). The selected area electron diffraction (SAED) shows an ordered array of spots recorded from [001] zone axis (Figure 1d, inset), confirming that SAL is of single crystallinity and preferentially enclosed by {002} top and bottom surfaces. The crystalline model of SAL from top and side views was schematically illuminated in Figure 1f. With H₂O₂ solution treatment for optimized 10 seconds, the sulfur atoms, which locate outermost in SAL, can be partially etched away from the surface to form V_S. The generation of V_S was confirmed with the electron paramagnetic resonance (EPR) spectra (Figure S4). The TEM image shows that the resulting V_S-SAL₁₀ displays no any morphology change in ultrathin structure (Figure S5). The corresponding EDS reveals that Ag, In,

and P contents were nearly stoichiometric 1:1:2 of AgInP_2S_6 , expect S element less than the stoichiometric ratio (Figure S6). It indicates that H_2O_2 treatment mainly leads to V_S , and has no etching effect on other moieties, which was also verified with the following XPS and the X-ray absorption near edge structure (XANES) spectra. The atomic resolution, aberration-corrected high-angle annular dark-field scanning TEM (HAADF-STEM) clearly reveals that considerable number of V_S were confined in the sheet (Figure 1e).

Full XPS spectra demonstrate the presence of Ag, In, P, S (Figure S7a). The high-resolution S 2p spectrum of BC shows the S 2p peak falling between 162 and 164 eV (Figure S7b), revealing -2 oxidation state of S. The S 2p peaks of SAL show dramatic low binding energy shift, compared with BC, and $\text{V}_\text{S}\text{-SAL}_{10}$ possesses further low-energy shift. The former shift may originate from exfoliation-resulting monolayerization,¹⁶ and the latter from V_S .¹⁵ As the decrease of binding energy indicates the enhanced electron screening effect due to the increase of the electron concentration,^{15,17} it implies that the electron density around the S sites increases in the sequence of BC, SAL, and $\text{V}_\text{S}\text{-SAL}_{10}$. It reveals that the residual S atoms exist in an electron oversaturated form and possess high electron density. No obvious change of binding energy of P elements was observed (Figure S7c), further demonstrating that the mechanical exfoliation and chemical etching only damage sulfur atoms and have little effect on P moiety. The pre-edge characteristic of the XANES spectra of the S K-edges of three AgInP_2S_6 were shown in Figure 2a, which could be fitted with components of a spin-orbit split. The spectra indicate the existence of main transitions energies between 2460 and 2500 eV, which originates from the excitation of an electron from a 1S inner orbital to a higher-energy orbital as a result of interaction with an X-ray. In comparison with BC, SAL shows a shift for S K-edge

peaks to lower energy side. This can be explained by the fact that the core electrons of S become more loosely bound after mechanical exfoliation due to the increased screening of the nuclear charge. Through V_S engineering, the S K-edge of V_S -SAL₁₀ can have a further small moving to lower energy side (Figure 2a). Moreover, the K-edge peak of P between 2100 to 2250 eV exhibits almost no differences among BC, SAL, and V_S -SAL₁₀ (Figure 2b), which is in good agreement with the above-mentioned XPS results.

The UV-vis diffuse reflectance spectra show that the band gap of SAL was determined 2.66 eV, a little larger than that of BC (2.31 eV) (Figure S8), exhibiting strong quantum size effect in the lateral direction. V_S -SAL₁₀ displays slightly narrowed bandgap (2.57 eV) with respect to SAL. It derives from that introduction of V_S may tailor the electronic structure of SAL through generating impurity states near the conduction band (CB) edge, which can be overlapped and delocalized with the CB minimum edge, leading to a reduced bandgap that may broaden the light absorption edge.^{18,19} The Mott-Schottky plots reveals that the CB edge of V_S -SAL₁₀ upshifts by ~ 0.06 eV and ~ 0.26 eV, relative to that of SAL and BC, respectively, as schematically illustrated in Figure S9. All BC, SAL, and V_S -SAL₁₀ were thus confirmed to possess suitable bandgaps as well as the appropriate band edge positions for photocatalytic CO₂ reduction under visible-light irradiation.

Photocatalytic performance of the AgInP₂S₆ related samples toward CO₂ photoreduction. The photocatalytic CO₂ conversion was carried out in the presence of water vapor under simulated solar irradiation (Figure 3). CO was detected the major product for BC and SAL (Figures 3a and 3b). BC shows the CO yield of 2.44 $\mu\text{mol g}^{-1}$ for the first hour and a trace amount of CH₄ of 0.63 $\mu\text{mol g}^{-1}$ (Figure 3a).

The photogenerated holes in the VB oxidize H₂O to produce hydrogen ions by the reaction of $\text{H}_2\text{O} \rightarrow 1/2\text{O}_2 + 2\text{H}^+ + 2\text{e}^-$. CO is formed by reacting with two protons and two electrons ($\text{CO}_2 + 2\text{e}^- + 2\text{H}^+ \rightarrow \text{CO} + \text{H}_2\text{O}$), and CH₄ formation through accepting eight electrons and eight protons ($\text{CO}_2 + 8\text{e}^- + 8\text{H}^+ \rightarrow \text{CH}_4 + 2\text{H}_2\text{O}$). SAL exhibits 6.9 and 14.3-time enhancement of production of CO and CH₄ relative to BC, reaching 17.1 $\mu\text{mol g}^{-1}$ and 9.0 $\mu\text{mol g}^{-1}$ for the first hour, respectively (Figure 3b). The prerogative of atomic ultrathin geometry of SAL may be mainly responsible for the enhanced photocatalytic activity besides larger surface area, allowing charge carriers to move from interior to the surface quickly to conduct catalysis, avoiding the recombination in body. Small amount of C₂H₄ was also detected for SAL with the yield of 5.3 $\mu\text{mol g}^{-1}$. C₂H₄ is generated through accepting twelve electrons and twelve protons ($2\text{CO}_2 + 12\text{e}^- + 12\text{H}^+ \rightarrow \text{C}_2\text{H}_4 + 4\text{H}_2\text{O}$). With the H₂O₂ etching process, excitingly, C₂H₄ excitingly becomes the main product for V_S-SAL₁₀ with the yield of 44.3 $\mu\text{mol g}^{-1}$ (Figure 3c). The calculated yield-based selectivity reaches ~73%, and the electron-based selectivity is as high as ~89%²⁰ (Figure 3e). Meanwhile, CO and CH₄ minority products were also traced with the yields of 10.9 $\mu\text{mol g}^{-1}$ and 5.6 $\mu\text{mol g}^{-1}$, respectively, both less than the case of SAL. It indicates that the surface of V_S-SAL₁₀ preferentially promotes the C₁ intermediates to C-C couple into C₂ product rather than liberate into free CO and CH₄ gases. The quantum yield of V_S-SAL₁₀ was measured 0.51 % at wavelength of 415 nm using monochromatic light (See the details in SI). The etching process time was found determinative for the dominant production of C₂H₄. The EPR measurement shows that the signal intensity

gradually increases with prolonging etching time from 5 seconds to 15 seconds (Figure S4), indicating being raised number of V_S in V_S -SAL. Elongation of the etching time from 5s to 10s was favorable for increasing yield of C_2H_4 (Figure S10). However, much long etching time of 15s decreases activity negatively, which may be due to that an excess of V_S defects may accelerate the recombination of photogenerated carriers.²¹ Reduction experiment of CO_2 preformed in the dark or absence of the photocatalyst shows no appearance of CO and hydrocarbon products, proving that the reduction reaction of CO_2 is driven by light under photocatalyst. Blank experiment with identical condition and in the absence of CO_2 shows no appearance of C_2H_4 , CO, and CH_4 , proving that the carbon source was completely derived from input CO_2 . An isotope labeling experiment using $^{13}CO_2$ confirms that the produced C_2H_4 originates from the input CO_2 (Figure S11a). The O_2 production was also detected using the similar isotope $H_2^{18}O$ tracer control experiment (Figure S11b).

Mechanism of the excellent photocatalytic performance of the V_S -SAL. DFT simulations were performed to explore the V_S -mediated catalytic selectivity mechanism toward CO and C_2H_4 on $AgInP_2S_6$. CO_2 molecules are initially adsorbed on the catalyst surface where H_2O molecules dissociate into hydroxyl and hydrogen ions at the same time. The free-energy profile for the photocatalytic CO_2 -to-hydrocarbon process with the lowest-energy pathway on the perfect $AgInP_2S_6$ surface was calculated, as shown in Figure 4. The key step for CO production is the hydrogenation of CO_2 to form $*COOH$, and the free-energy change of the step is 0.48 eV. Subsequently, the reaction intermediate ($*COOH$) further couples a

proton/electron pair to generate CO and H₂O molecules. An adsorption energy of -0.07 eV of the produced *CO on the defect-free AgInP₂S₆ surface implies the physical adsorption on the catalyst (Figure S12a). It means that *CO molecules can easily liberate from BC and SAL to become free CO gas, allowing high CO catalytic selectivity. Additional parts of *CO were continuously reduced by the incoming electrons and the successive protonation process to transform into CH₄.^{19,22} While the charge density of the valence band (VB) for pristine AgInP₂S₆ is evenly located on all the S and Ag atoms, contrastingly, the charge density of the VB is mainly located on the Ag atoms near the V_S for V_S-AgInP₂S₆, (Figure S13). That is to say, the presence of V_S in V_S-AgInP₂S₆ causes the charge enrichment on the Ag atoms near the V_S, which would benefit for stabilizing the reaction intermediates. For V_S-SAL, V_S can act as a trap for the *CO molecule, that is, the *CO molecule can chemically adsorb at exposed Ag sites with an adsorption energy of -0.25 eV (CO can only physically adsorb on the exposed P and In sites with distance of 2.56 and 3.20 Å, See Figure S13b-13d). The higher CO onset desorption temperature on V_S-SAL₁₀ than SAL affirms the stronger absorption (Figure S14). The absorbed *CO can be further protonated to successively form a series of key reaction intermediates with unsaturated coordination, which was confirmed with *in-situ* FTIR measurement (Figure S15). The other *CO molecules produced on the surface diffuses toward V_S and couple with those reaction intermediates to produce C₂H₄. The C₂H₄ free energy diagrams are summarized in Figure 4c, while the corresponding C-C coupling barriers are presented in Figure 4b. The different C-C coupling energy barriers were evaluated for three unsaturated reaction intermediates (*COH, *CHOH, and *CH₂) (Figure 4b). The coupling energy barrier with a value of 0.84 eV (*CO-CHOH) is lower than that of other coupling pathways (*CO-COH, 1.01 eV and *CO-CH₂, 1.84 eV), hence the

C₂H₄ will be produced via CO-CHOH coupling and hydrogenation. The whole free energy diagram shows that the process of *CO to *COH is regarded as the potential determining-step (0.86 eV). It should be especially emphasized that the detected small amount of C₂H₄ on SAL possibly originates from potential existence of the tiny number of V_S in SAL, resulting from mechanically detaching sulfur atoms from SAL during the probe sonication exfoliation process. The reaction process for reduction of CO₂ into C₂H₄, CO, and CH₄ over V_S-SAL under light illumination is thus proposed in Figure S16.

Surface photovoltage spectroscopy (SPV) was employed to study separation and transport behavior of photoinduced charge carriers of the studied AgInP₂S₆. More negative SPV signal change reflects higher concentration of photogenerated electrons before and after light illumination. All BC, SAL, and V_S-SAL₁₀ show the SPV response under light illumination (Figures 5 and S17), corresponding to band-to-band transition. The SAL and BC exhibit 20 ~ 30 mV and 5 ~ 10 mV negative change before and after light illumination, respectively. More negative SPV signal change of SAL than BC exactly demonstrates that the atomically thin structure enables to alleviate the bulk electron-hole recombination to achieve high-concentration accumulation of photogenerated electrons on the surface. The V_S-SAL₁₀ display obviously dramatic change of 50 ~ 60 mV, indicating that introduction of V_S can further favor the carrier separation and allow much increment of electron concentration on the surface. The excess surviving electrons are not only the necessary prerequisite to photoconversion of CO₂, but also can promote CO₂ adsorption and activation on the surface of the photocatalyst.

Photoluminescence (PL) decay profiles show that the SAL (~ 1.32 ns) possesses longer PL lifetime than BC (~ 0.40 ns) (Figure S18), demonstrating that the

atomically thin structure can indeed shorten transfer distance of the carriers and decrease recombination chance of electron and hole in the body. V_S -SAL₁₀ exhibits the longest PL lifetime (~ 1.50 ns), confirming that the surface V_S can serve as surface separation centers for charge carriers and further promote the charge separation, therefore offering more opportunities for photocatalytic CO₂ reduction. Transient photocurrent shows that the photocurrent intensity of SAL was enhanced with steadily repeating course due to promoted charge separation, compared with BC (Figure S19a). The highest photocurrent intensity of V_S -SAL₁₀ implies that the V_S also makes effective contribution for saving carriers. Electrochemical impedance spectra (EIS) reveal that V_S -SAL₁₀ manifests the smallest semicircle in Nyquist plots (Figure S19b), suggesting the lowest charge-transfer resistance, which permits fast transport of photoinduced charge.

Discussion

In summary, single atomically-thin AgInP₂S₆ layers were successfully synthesized through a facile probe sonication exfoliation of BC. The atomically thin structure of SAL, relative to BC, enables more charge carriers to mobile from the interior onto the surface and survivingly accumulate onto the active sites to improve the photocatalytic activity. While SAL exhibits obvious conversion efficiency with CO as the major product, the presence of V_S in V_S -SAL changes the CO₂ photoreduction pathway to allow the dominant generation of C₂H₄. This work not only paves an effective approach for selectively producing multi-carbon product from CO₂ photoreduction but also provides a new insight for catalyst design through vacancy defect engineering.

Methods

Synthesis of BC, SAL and V_S-SAL. The AgInP₂S₆ crystals have been synthesized by physical vapor transport (PVT) in a two-zone furnace. Stoichiometric amounts of high-purity elements (mole ratio Ag : In : P : S = 1:1:2:6, around 1 g in total) were sealed into a quartz ampoule with the pressure of 1×10^{-4} Torr inside the ampoule. The length of the quartz ampoule was about 15–18 cm with the 13mm external diameter. The ampoule was kept in a two-zone furnace (680 → 600 °C) for 1 week.²³ After the furnace was cooled down to room temperature, the AgInP₂S₆ crystalline powders could be found inside the ampoule (Figure S1a). SAL were prepared by sonication-assisted liquid exfoliation processes from synthetic AgInP₂S₆ crystalline powders. SAL was immersed in H₂O₂ solutions with the of concentrations 0.1 mol/L inside which SAL were allowed to react with H₂O₂ for 5, 10, 15 s, referred to V_S-SAL₅, V_S-SAL₁₀ and V_S-SAL₁₅, respectively, at 25 °C. All the obtained samples were carefully washed and dried before use.

Characterizations. X-ray diffraction (XRD) (Rigaku Ultima III, Japan) was used to investigate the purity information and crystallographic phase of the as-prepared powder samples. The XRD pattern was recorded by using Cu-ka radiation ($\lambda = 0.154178$ nm) at 40 kV and 40 mA with a scan rate of $10^\circ \text{ min}^{-1}$. The morphology was characterized by the field emission scanning electron microscopy (FESEM, FEI NOVA NANOSEM 230). The transmission electron microscopy (TEM) and fine resolution transmission electron microscope (HRTEM) images were taken on a JEM 200CX TEM apparatus. X-ray photoelectron spectroscopy (XPS; K-Alpha, Thermo

Fisher Scientific) was standardized according to the binding energy of the adventitious C 1s peak at 284.8 eV, which was used to inspect the chemical states. A UV-vis spectrophotometer (UV-2550, Shimadzu) was hired to record the UV-visible diffuse reflectance spectra and switched to the absorption spectrum on the basis of the Kubelka–Munk connection at room temperature. Fourier transform infrared (FTIR) spectroscopy was examined using a Nicolet NEXUS870 (USA) spectrometer. The photoluminescence decay profile was described by the single-particle confocal fluorescence spectroscopy measurement (PicoHarp300). Surface photovoltage spectroscopy (SPV) was detected through AFM (Asylum Research, MFP-3D-SA, USA) analysis with the photo-assisted (a 405 nm laser excitation) Kelvin probe force microscopy (KPFM). Photoelectrochemical measurements were detected by a CHI660E electrochemical workstation using a standard three-electrode system in 1 mM NaSO₄ solution. Soft X-ray absorption spectra (XAS) were collected from the Soft X-ray Spectroscopy beamline at the Australian Synchrotron(AS, Australia), part of ANSTO.

Measurement of Photocatalytic Activity. For the photocatalytic reduction of CO₂, 4~5 mg of sample was uniformly dispersed on the glass reactor with an area of 4.2 cm². A 300 W Xenon arc lamp was used as the light source of photocatalytic reaction. The volume of reaction system was about 460 ml. Before the irradiation, the system was vacuum-treated several times, and then the high purity of CO₂ gas was followed into the reaction setup for reaching ambient pressure. 0.4 mL of deionized water was injected into the reaction system as reducer. The as-prepared photocatalysts were

allowed to equilibrate in the CO₂/H₂O atmosphere for several hours to ensure that the adsorption of gas molecules was complete. During the irradiation, about 1 mL of gas was continually taken from the reaction cell at given time intervals for subsequent CO, CH₄ and C₂H₄ concentration analysis by using a gas chromatograph (GC-2014C, Shimadzu Corp., Japan).

The external quantum efficiency (EQE): The quantum yield was calculated according to the below equation:

$$E_Q = N(\text{electron}) / N(\text{photon})$$
$$= [N(\text{CO}) \times 2 + N(\text{CH}_4) \times 8 + N(\text{C}_2\text{H}_4) \times 12] / N(\text{photon}) \times 100\%$$

where N (electron) signify two electrons are required to produce one molecule CO in unit time. The N (photon) is figured out according to the equation:

$$N(\text{photon}) = [\text{Light intensity} \times \text{Illumination area} \times \text{Time}] / [\text{Average single photon energy} \times N_A]$$

A light-emitting diodes (LEDs) provides the monochromatic incident light with identical condition. The light intensity of LEDs with 415 nm wavelength is 10.5mW/cm², the illumination area is controlled to 4.91 cm², N_A is the Avogadro constant, and the average single photon energy is calculated according to the equation:

$$E(\text{photon}) = hc / \lambda$$

in which h is the Planck constant, c indicates speed of light, and λ is the wavelength.

Computational details: The density functional theory (DFT) calculations were made with the Vienna Ab Initio Simulation Package^{24,25} (VASP) code. The

exchange-correlation interactions and the ion-electron interactions were solved by the Perdew-Burke-Ernzerhof (PBE) functionals^{26,27} and the projector-augmented wave (PAW) method²⁸, respectively. The monolayer AgInP₂S₆ was a model with a 2 × 2 supercell. A plane-wave cutoff of 450 eV was adopted and the maximal force on all-atom was below 0.02 eV/Å. The distance between periodic units in the vertical direction was larger than 16 Å. The DFT-D2 method of Grimme²⁹ was used in all calculations to accurately describe long-range Van der Waals (vdW) interactions. The climbing-image nudged elastic band (CI-NEB) method³⁰ incorporated with spin-polarized DFT was used to locate the minimum-energy path. The intermediate images of each CI-NEB simulation were relaxed until the perpendicular forces were smaller than 0.1eV/Å.

The free energies of each reaction intermediates were determined according to $G = E + ZPE - TS$. The electronic energies (E) can be directly obtained from DFT computations. The zero-point energy (ZPE) and entropy correction (TS) were calculated from vibration analysis by standard methods. The computational hydrogen electrode (CHE) model³¹ was used to treat the free energy change of each reaction step involving a proton-electron pair transfer. In this model, the free energy of a proton-electron pair at 0 V vs RHE is equal to half of the free energy of hydrogen molecule.

References

1. Tu, W.; Zhou, Y.; Zou, Z. Photocatalytic Conversion of CO₂ into Renewable Hydrocarbon Fuels: State-of-the-Art Accomplishment, Challenges, and Prospects. *Adv. Mater.* **26**, 4607–4626 (2014).
2. Chen, G. B.; Waterhouse, G. I. N.; Shi, R.; Zhao, J. Q.; Li, Z. H.; Wu, L. Z.; Tung, C. H.; Zhang, T. R. From Solar Energy to Fuels: Recent Advances in Light-Driven C-1 Chemistry, *Angew. Chem. Int. Ed.* **58**, 17528-17551 (2019).
3. Liu, Q.; Zhou, Y.; Kou, J. H.; Chen, X. Y.; Tian, Z. P.; Gao, J.; Yan, S. C.; Zou, Z. G. High-Yield Synthesis of Ultralong and Ultrathin Zn₂GeO₄ Nanoribbons toward Improved Photocatalytic Reduction of CO₂ into Renewable Hydrocarbon Fuel. *J. Am. Chem. Soc.* **132**, 14385-14387 (2010).
4. Han, Q. T.; Bai, X. W.; Man, Z. Q.; He, H. C.; Li, L.; Hu, J. Q.; Alsaedi, A.; Hayat, T.; Yu, Z. T.; Zhang, W. H. *J. Am. Chem. Soc.* **141**, 4209-4213 (2019).
5. Tu, W. G.; Zhou, Y.; Liu, Q.; Yan, S. C.; Bao, S. S.; Wang, X. Y.; Wang, X. Y.; Xiao, M.; Zou, Z. G. An In Situ Simultaneous Reduction-Hydrolysis Technique for Fabrication of TiO₂-Graphene 2D Sandwich-Like Hybrid Nanosheets: Graphene-Promoted Selectivity of Photocatalytic-Driven Hydrogenation and Coupling CO₂ into Methane and Ethane. *Adv. Funct. Mater.* **23**, 1743-1749 (2013).
6. Jiang, W.; Low, J.; Mao, K.; Duan, D.; Chen, S.; Liu, W.; Pao, C.-W.; Ma, J.; Sang, S.; Shu, C.; Zhan, X.; Qi, Z.; Zhang, H.; Liu, Z.; Wu, X.; Long, R.; Song, L.; Xiong, Y. Pd-Modified ZnO–Au Enabling Alkoxy Intermediates Formation and Dehydrogenation for Photocatalytic Conversion of Methane to Ethylene. *J. Am. Chem.*

Soc. **143**, 269-278 (2021).

7. Bai, W.; Hu, Z.; Xiao, C.; Xiao, C.; Guo, J.; Li, Z.; Zou, Y.; Liu, X.; Zhao, J.; Tong, W.; Yan, W.; Qu, Z.; Ye, B.; Xie, Y.; Xie, Y. Parasitic Ferromagnetism in Few-Layered Transition-Metal Chalcogenophosphate. *J. Am. Chem. Soc.* **142**, 10849–10855 (2020).

8. Vysochanskii, Y.; Glukhov, K.; Maior, M.; Fedyo, K.; Kohutych, A.; Betsa, V.; Prits, I.; Gurzan, M. Ferroelectric and Semiconducting Properties of Sn₂P₂S₆ Crystals with Intrinsic Vacancies. *Ferroelectrics* **418**, 124–133 (2011).

9. Babuka, T.; Glukhov, K.; Vysochanskii, Y.; Makowska-Janusik, M. Structural, Electronic, Vibration and Elastic Properties of the Layered AgInP₂S₆ Semiconducting Crystal-DFT Approach. *RSC Adv.* **8**, 6965–6977 (2018).

10. Dziaugys, A.; Banys, J.; MacUtkevic, J.; Vysochanskii, J. Conductivity Spectroscopy of New AgInP₂S₆ Crystals. *Integr. Ferroelectr.* **103**, 52–59 (2008).

11. Wang, X.; Du, K.; Liu, W.; Hu, P.; Lu, X.; Xu, W.; Kloc, C.; Xiong, Q. Second-Harmonic Generation in Quaternary Atomically Thin Layered AgInP₂S₆ Crystals. *Appl. Phys. Lett.* **109**, (2016).

12. Huang, B.; McGuire, M. A.; May, A. F.; Xiao, D.; Jarillo-Herrero, P.; Xu, X. D. Emergent Phenomena and Proximity Effects in Two-Dimensional Magnets and Heterostructures. *Nat. Mater.* **19**, 1276-1289 (2020).

13. Wang, L. M.; Chen, W. L.; Zhang, D. D.; Du, Y. P.; Amal, R.; Qiao, S. Z.; Bf, J. W.; Yin, Z. Y. Surface Strategies for Catalytic CO₂ Reduction: from Two-Dimensional Materials to Nanoclusters to Single Atoms. *Chem. Soc. Rev.* **48**, 5310-5349 (2019).

14. Chen, S.; Wang, H.; Kang, Z.; Jin, S.; Zhang, X.; Zheng, X.; Qi, Z.; Zhu, J.; Pan,

- B.; Xie, Y. Oxygen Vacancy Associated Single-Electron Transfer for Photofixation of CO₂ to Long-Chain Chemicals. *Nat. Commun.* **10**, 788 (2019).
15. Wang, X.; Zhang, Y.; Si, H.; Zhang, Q.; Wu, J.; Gao, L.; Wei, X.; Sun, Y.; Liao, Q.; Zhang, Z.; Ammarah, K.; Gu, L.; Kang, Z.; Zhang, Y. Single-Atom Vacancy Defect to Trigger High-Efficiency Hydrogen Evolution of MoS₂. *J. Am. Chem. Soc.* **142**, 4298–4308 (2020).
16. Liang, H.; Meng, F.; Cabán-Acevedo, M.; Li, L.; Forticaux, A.; Xiu, L.; Wang, Z.; Jin, S. Hydrothermal Continuous Flow Synthesis and Exfoliation of NiCo Layered Double Hydroxide Nanosheets for Enhanced Oxygen Evolution Catalysis. *Nano Lett.* **15**, 1421–1427 (2015).
17. Zhu, M.; Kim, S.; Mao, L.; Fujitsuka, M.; Zhang, J.; Wang, X.; Majima, T. Metal-Free Photocatalyst for H₂ Evolution in Visible to Near-Infrared Region: Black Phosphorus/Graphitic Carbon Nitride. *J. Am. Chem. Soc.* **139**, 13234–13242 (2017).
18. Zhang, N.; Jalil, A.; Wu, D.; Chen, S.; Liu, Y.; Gao, C.; Ye, W.; Qi, Z.; Ju, H.; Wang, C.; Wu, X.; Song, L.; Zhu, J.; Xiong, Y. Refining Defect States in W₁₈O₄₉ by Mo Doping: A Strategy for Tuning N₂ Activation towards Solar-Driven Nitrogen Fixation. *J. Am. Chem. Soc.* **140**, 9434–9443 (2018).
19. Li, X.; Sun, Y.; Xu, J.; Shao, Y.; Wu, J.; Xu, X.; Pan, Y.; Ju, H.; Zhu, J.; Xie, Y. Selective Visible-Light-Driven Photocatalytic CO₂ Reduction to CH₄ Mediated by Atomically Thin CuIn₅S₈ Layers. *Nat. Energy* **4**, 690–699 (2019).
20. Das, S.; Perez-Ramirez, J.; Gong, J. L.; Dewangan, N.; Hidajat, K.; Gates, B. C.; Kawi, S. Core-shell structured catalysts for thermocatalytic, photocatalytic, and

electrocatalytic conversion of CO₂, *Chem. Soc. Rev.* **49**, 2937-3004 (2020). The electron-based selectivity is calculated, for example, selectivity (CO) = $[2n(\text{CO})/2n(\text{CO}) + 8n(\text{CH}_4) + 12n(\text{C}_2\text{H}_4)]$.

21. Wendumu, T. B.; Seifert, G.; Lorenz, T.; Joswig, J. O.; Enyashin, A. Optical Properties of Triangular Molybdenum Disulfide Nanoflakes. *J. Phys. Chem. Lett.* **5**, 3636–3640 (2014).

22. Gao, G.; Jiao, Y.; Waclawik, E. R.; Du, A. Single Atom (Pd/Pt) Supported on Graphitic Carbon Nitride as an Efficient Photocatalyst for Visible-Light Reduction of Carbon Dioxide. *J. Am. Chem. Soc.* **138**, 6292–6297 (2016).

23. Wang, X.; Du, K.; Liu, W.; Hu, P.; Lu, X.; Xu, W.; Kloc, C.; Xiong, Q. Second-Harmonic Generation in Quaternary Atomically Thin Layered AgInP₂S₆ Crystals. *Appl. Phys. Lett.* **109** (2016).

24. Kresse, G.; Furthmüller, J. Efficient Iterative Schemes for Ab Initio Total-Energy Calculations Using a Plane-Wave Basis Set. *Phys. Rev. B*, **54**, 11169–11186 (1996).

25. Kresse, G.; Joubert, D. From Ultrasoft Pseudopotentials to the Projector Augmented-Wave Method. *Phys. Rev. B* **59**, 1758–1775 (1999).

26. Perdew, J. P.; Chevary, J. A.; Vosko, S. H.; Jackson, K. A.; Pederson, M. R.; Singh, D. J.; Fiolhais, C. Atoms, Molecules, Solids, and Surfaces: Applications of the Generalized Gradient Approximation for Exchange and Correlation. *Phys. Rev. B* **46**, 6671–6687 (1992).

27. Perdew, J. P.; Wang, Y. Accurate and Simple Analytic Representation of the Electron-Gas Correlation Energy. *Phys. Rev. B* **45**, 13244–13249 (1992).

28. Blöchl, P. E. Projector Augmented-Wave Method. *Phys. Rev. B* **50**, 17953–17979 (1994).
29. Grimme, S. Semiempirical GGA-Type Density Functional Constructed with a Long-Range Dispersion Correction. *J. Comput. Chem.* **27**, 1787–1799 (2006).
30. Henkelman, G.; Uberuaga, B. P.; Jónsson, H. A Climbing Image Nudged Elastic Band Method for Finding Saddle Points and Minimum Energy Paths. *J. Chem. Phys.* **113**, 9901–9904 (2000).
31. Nørskov, J. K.; Rossmeisl, J.; Logadottir, A.; Lindqvist, L.; Kitchin, J. R.; Bligaard, T.; Jónsson, H. Origin of the Overpotential for Oxygen Reduction at a Fuel-Cell Cathode. *J. Phys. Chem. B*, **108**, 17886–17892 (2004).

Acknowledgement

The authors wish to acknowledge the support of National Key R &D Program of China (2018YFE0208500), 973 program (2017YFA0204800), NSF of China (21972065, 21773114, and 21773027), the Fundamental Research Funds for the Central University (020414380167), NSF of Jiangsu Province (No. BK20171246), the Hefei National Laboratory for Physical Sciences at the Microscale (KF2020006), the Program for Guang-dong Introducing Innovative and Entrepreneurial Team (2019ZL08L101) and The university Development Fund (UDF01001159).

Author contributions

Y. Z., Y. X. and Z. Z instructed this work. L. S. and J. W. carried out the DFT calculation. W. G., H. H., X. Li, Z. C., Y. Y., and Q. S. performed the experiments and co-wrote this manuscript. X. W. contributed the PL spectrum measurement.

Competing interests: The authors declare on Competing Financial or Non-Financial Interests.

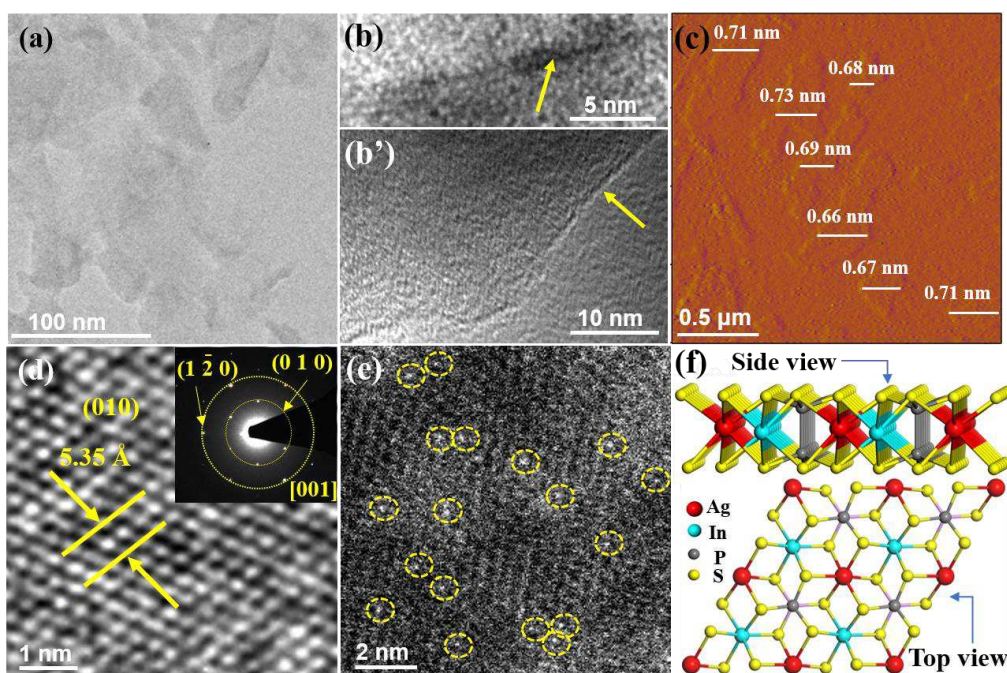


Fig. 1 TEM images of (a) SAL, (b) vertically standing and (b') laying single piece SAL, (c) AFM image of SAL showing an average thickness of ~ 0.69 nm. (d) HRTEM image and the EDS. (e) HAADF-STEM image of V_S -SAL₁₀, in which the atomically dispersed V_S are highlighted with the yellow circles. (f) The crystalline models of SAL from top and side views.

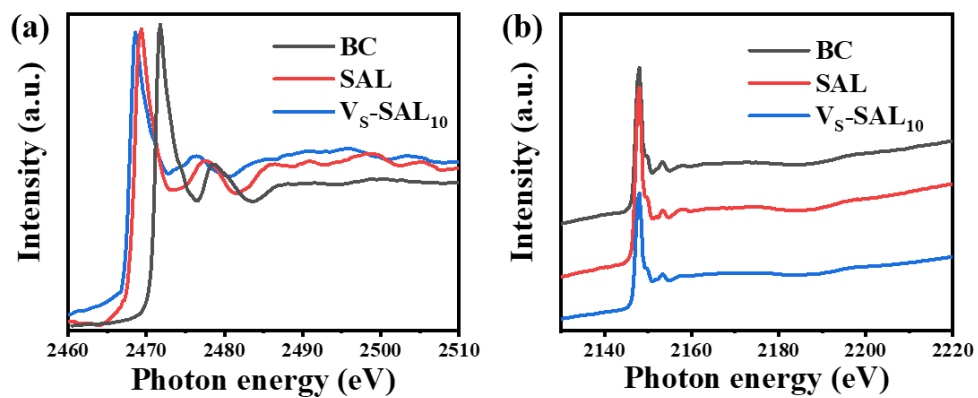


Fig. 2 (a) S and (b) P K-edge XANES spectra of BC, SAL, and Vs-SAL₁₀.

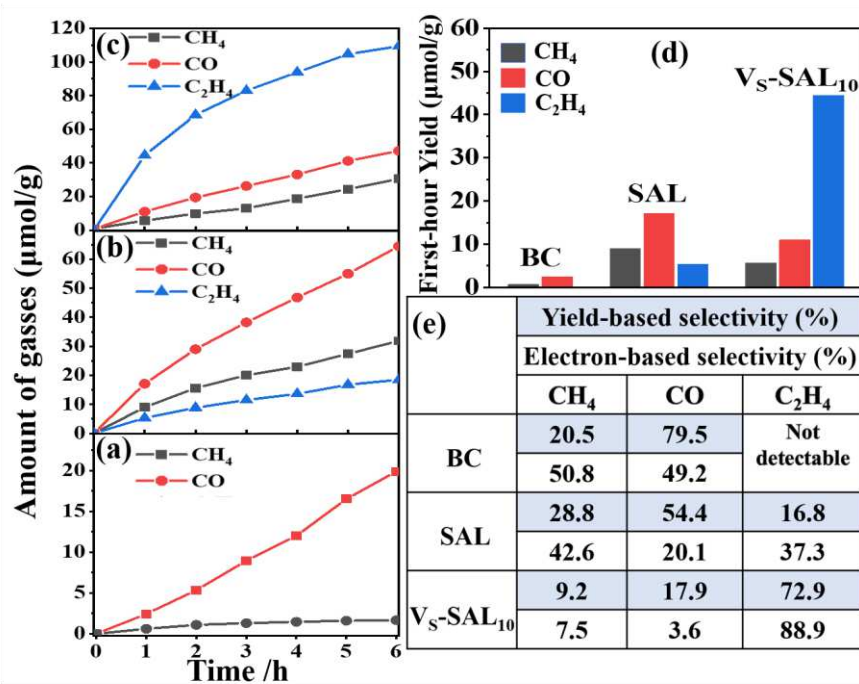


Fig. 3 Photocatalytic gases evolution amounts as a function of light irradiation times of (a) BC, (b) SAL, and (c) V_S-SAL. (d) Photocatalytic activity for the first hour. (e) Table illustration for the yield and electron-based selectivities of photocatalytic CO₂ conversion.

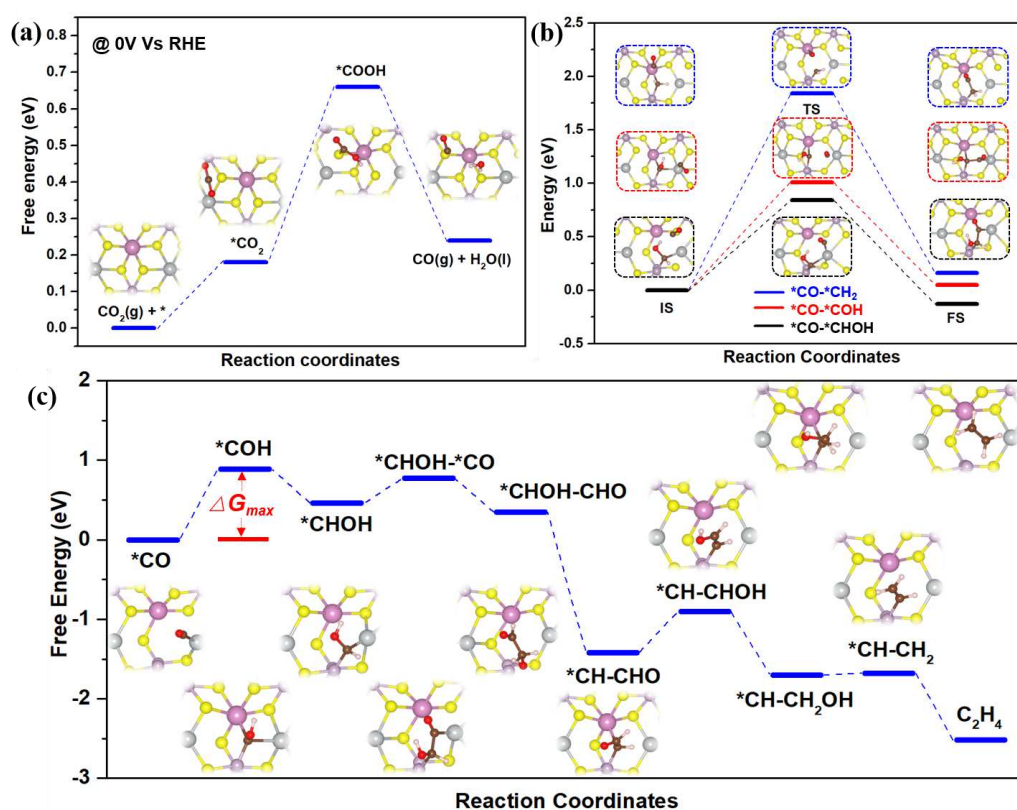


Fig. 4 (a) Gibbs free energy diagrams for CO₂ reduction to CO over perfect AgInP₂S₆. (b) Three kinds of possible C-C coupling pathways over AgInP₂S₆ containing V_s. (c) Gibbs free energy diagrams for CO reduction to C₂H₄ over AgInP₂S₆ with V_s. The insets show the corresponding optimized geometries for the reaction intermediates during the CO₂ reduction process. Sulfur, phosphorus, indium, silver, carbon, oxygen, and hydrogen atoms are yellow, purple, lilac, gray, black, red, and white, respectively.

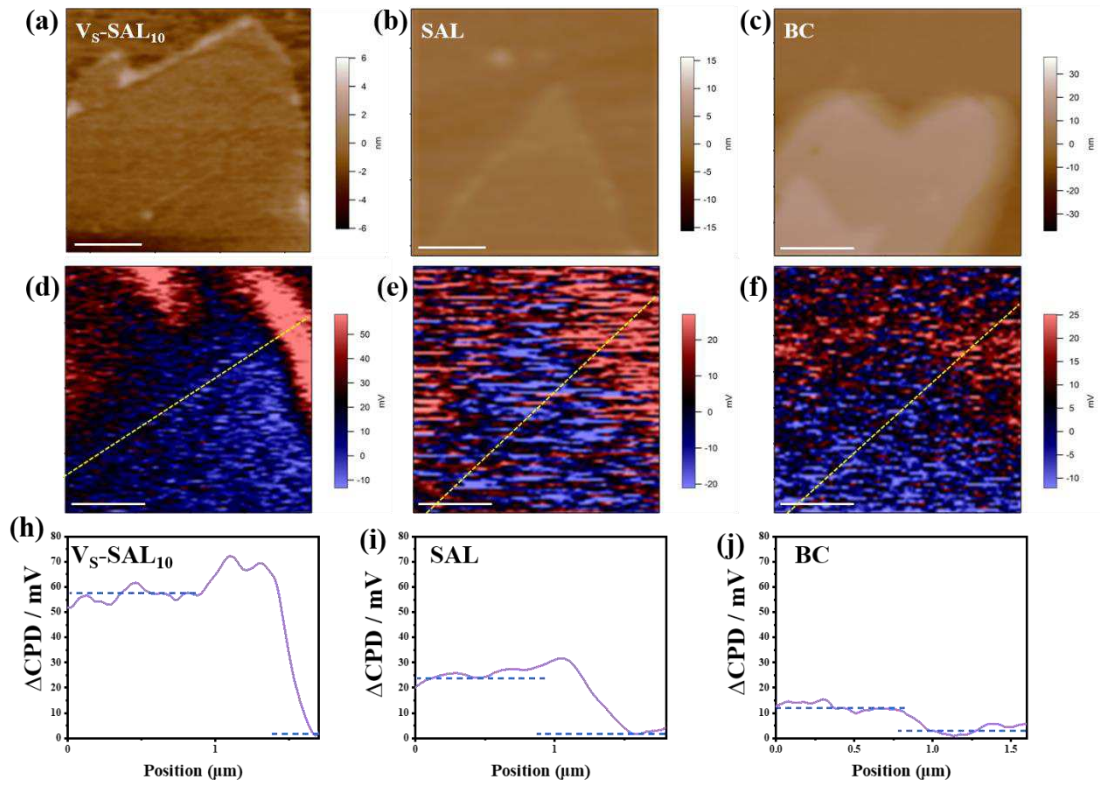


Figure 5. Height images of (a) V_S -SAL₁₀, (b) SAL and (c) BC; The SPV images (d) V_S -SAL₁₀, (e) SAL and (f) BC in (a), (b) and (c), respectively, are differential images between potential images under light and in the dark. All scale bars represent 0.5 μm . The surface photovoltage change by subtracting the potential under dark conditions from that under illumination (SPV, $\Delta\text{CPD} = \text{CPD dark} - \text{CPD light}$) of (h) V_S -SAL₁₀, (i) SAL and (j) BC.

Figures

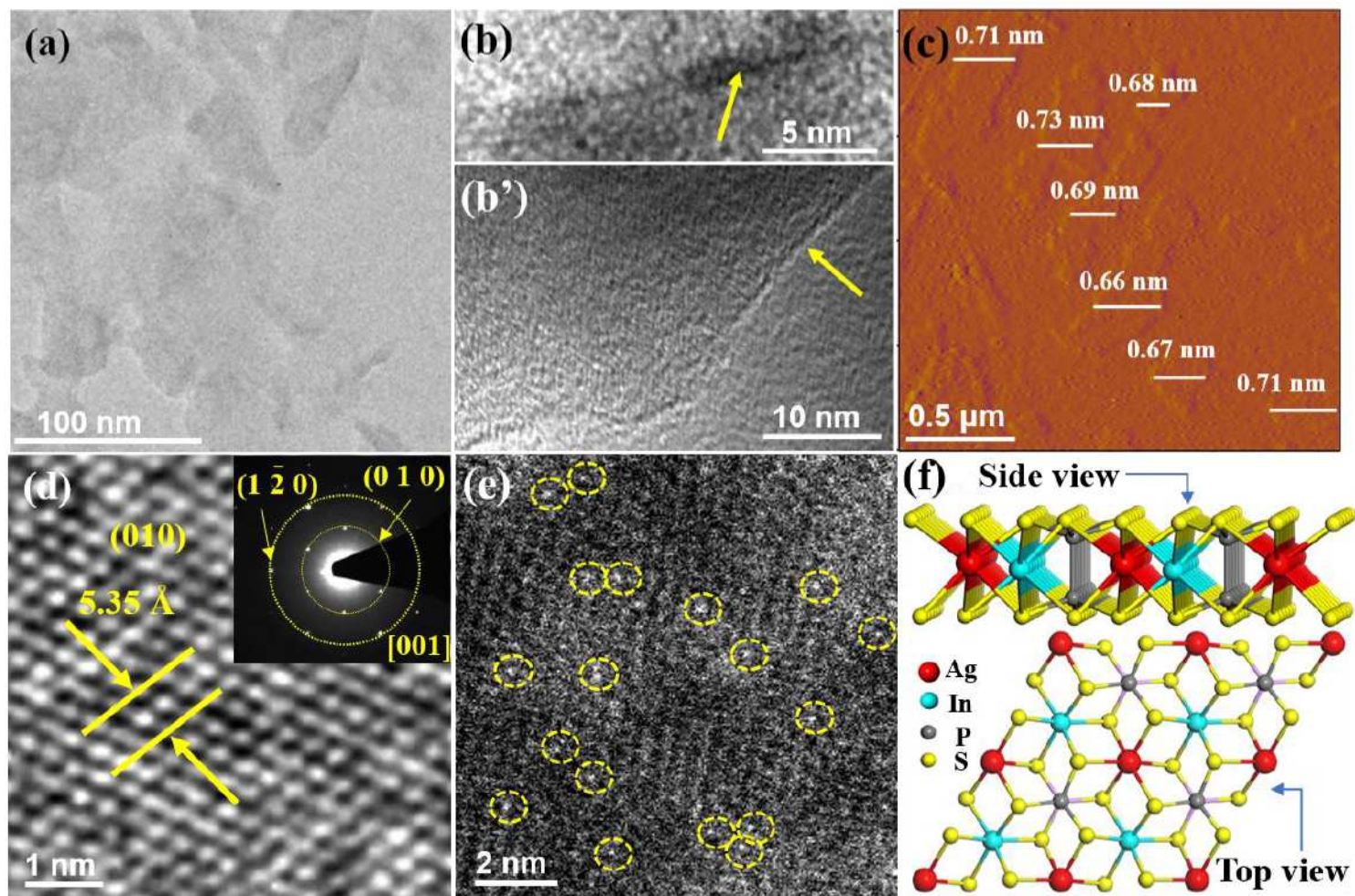


Figure 1

TEM images of (a) SAL, (b) vertically standing and (b') laying single piece SAL, (c) AFM image of SAL showing an average thickness of ~ 0.69 nm. (d) HRTEM image and the EDS. (e) HAADF-STEM image of VS-SAL10, in which the atomically dispersed Vs are highlighted with the yellow circles. (f) The crystalline models of SAL from top and side views.

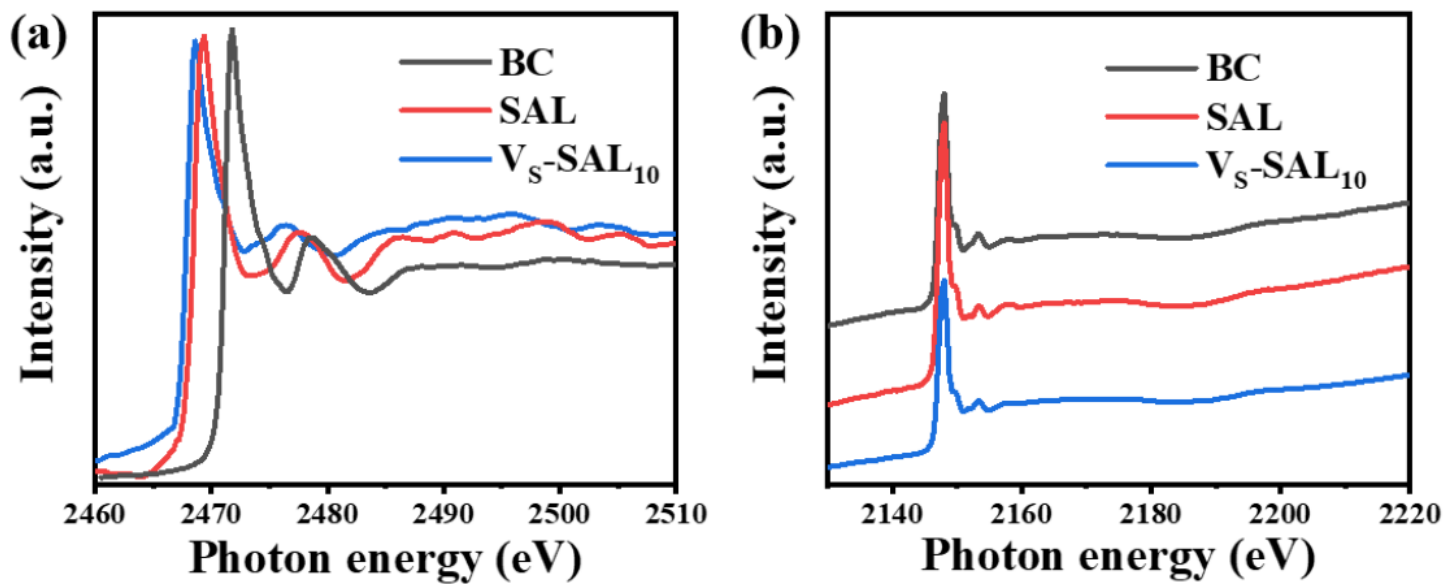


Figure 2

(a) S and (b) P K-edge XANES spectra of BC, SAL, and Vs-SAL10.

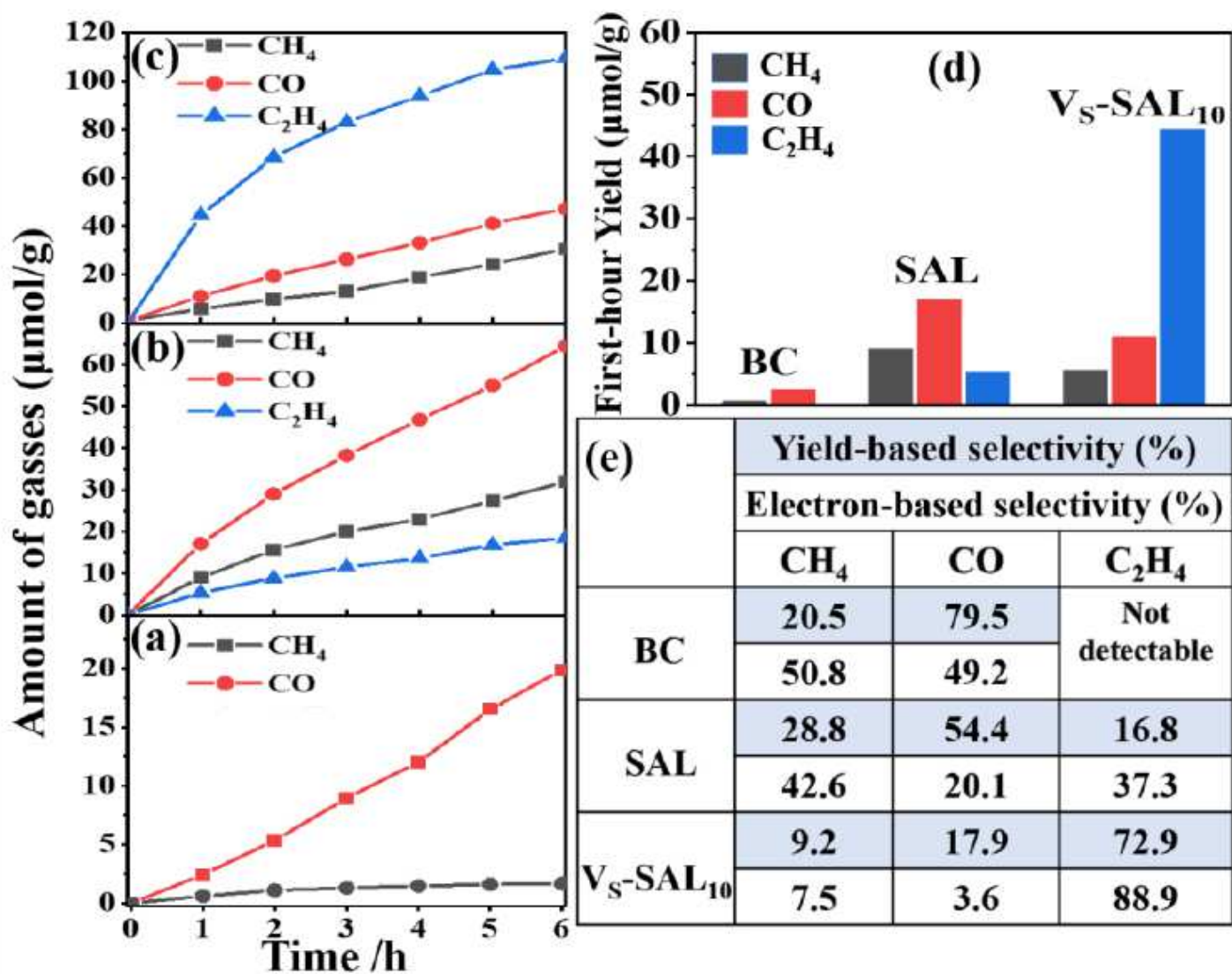


Figure 3

Photocatalytic gases evolution amounts as a function of light irradiation times of (a) BC, (b) SAL, and (c) VS-SAL. (d) Photocatalytic activity for the first hour. (e) Table illustration for the yield and electron-based selectivities of photocatalytic CO₂ conversion.

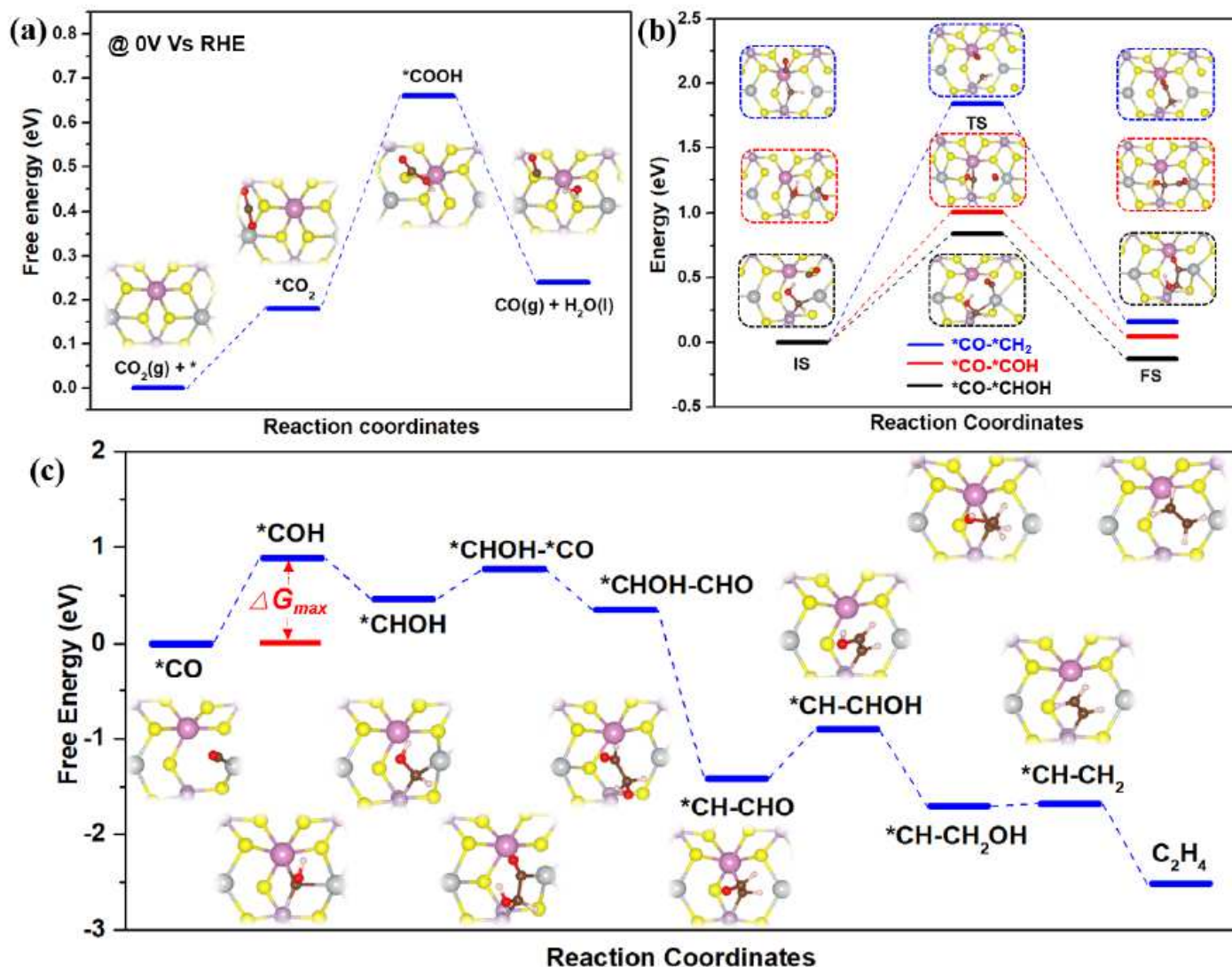


Figure 4

(a) Gibbs free energy diagrams for CO₂ reduction to CO over perfect AgInP₂S₆. (b) Three kinds of possible C-C coupling pathways over AgInP₂S₆ containing Vs. (c) Gibbs free energy diagrams for CO reduction to C₂H₄ over AgInP₂S₆ with Vs. The insets show the corresponding optimized geometries for the reaction intermediates during the CO₂ reduction process. Sulfur, phosphorus, indium, silver, carbon, oxygen, and hydrogen atoms are yellow, purple, lilac, gray, black, red, and white, respectively.

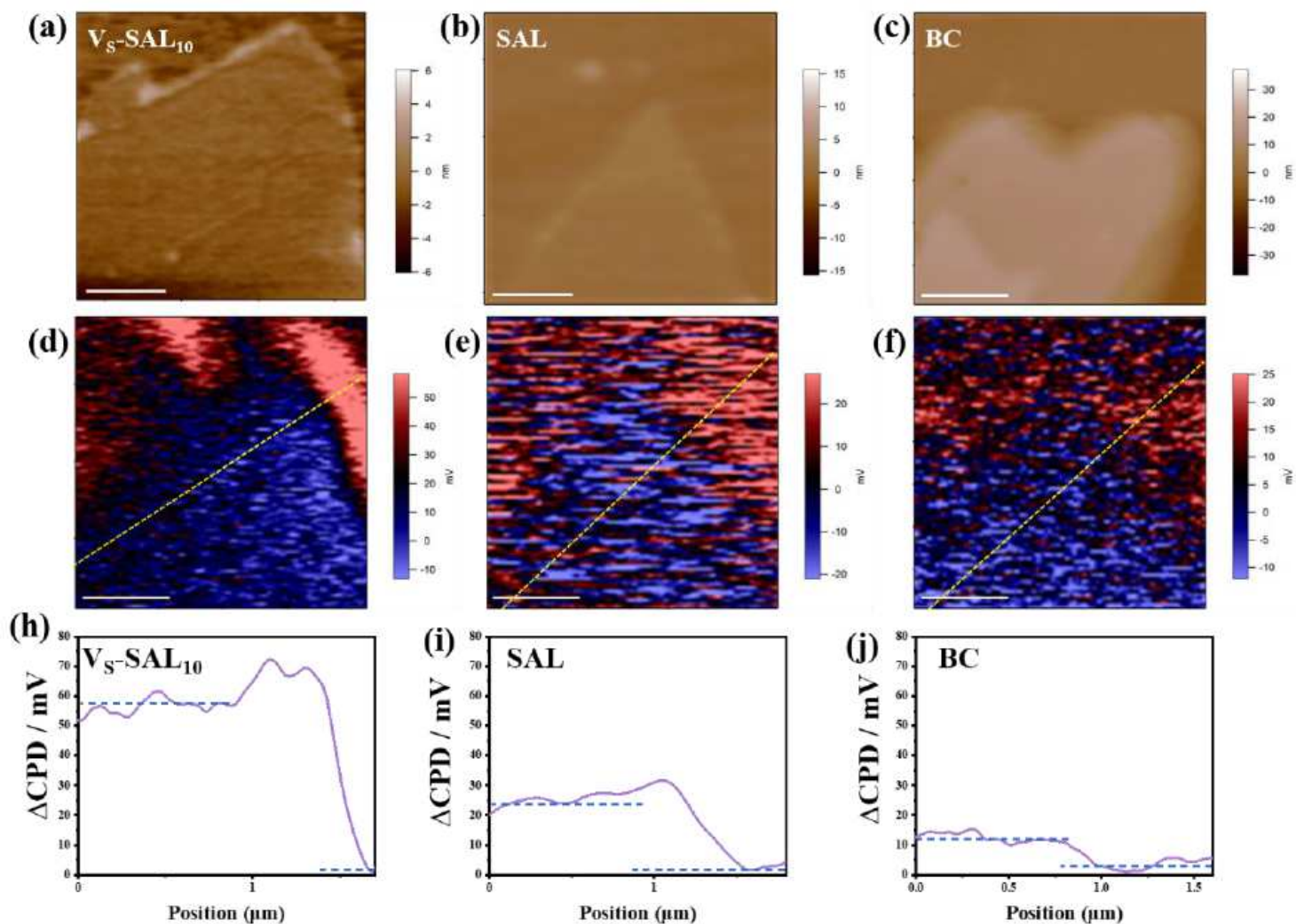


Figure 5

Height images of (a) VS-SAL₁₀, (b) SAL and (c) BC; The SPV images (d) VS-SAL₁₀, (e) SAL and (f) BC in (a), (b) and (c), respectively, are differential images between potential images under light and in the dark. All scale bars represent 0.5 μm. The surface photovoltage change by subtracting the potential under dark conditions from that under illumination (SPV, $\Delta\text{CPD} = \text{CPD dark} - \text{CPD light}$) of (h) VS-SAL₁₀, (i) SAL and (j) BC.

Supplementary Files

This is a list of supplementary files associated with this preprint. Click to download.

- [Slnc.pdf](#)